

## NUMERICAL INVESTIGATION OF TWO ELEMENT CAMBER MORPHING AIRFOIL IN LOW REYNOLDS NUMBER FLOWS

RAJESH SENTHIL KUMAR T.\*, V. SIVAKUMAR,  
BALAJEE RAMAKRISHNANANDA, ARJHUN A.K, SURIYAPANDIYAN

Department of Aerospace Engineering, Amrita School of Engineering Coimbatore, Amrita  
Vishwa Vidyapeetham, Amrita University, 641112, Tamil Nadu, India

\*Corresponding Author: t\_rajesh@cb.amrita.edu

### Abstract

Aerodynamic performance of a two-element camber morphing airfoil was investigated at low Reynolds number using the transient SST model in ANSYS FLUENT 14.0 and  $e^N$  method in XFLR5. The two-element camber morphing concept was employed to morph the baseline airfoil into another airfoil by altering the orientation of mean-line at 35% of the chord to achieve better aerodynamic efficiency. NACA 0012 was selected as baseline airfoil. NACA 23012 was chosen as the test case as it has the camber-line similar to that of the morphed airfoil and as it has the same thickness as that of the baseline airfoil. The simulations were carried out at chord based Reynolds numbers of  $2.5 \times 10^5$  and  $3.9 \times 10^5$ . The aerodynamic force coefficients, aerodynamic efficiency and the location of the transition point of laminar separation bubble over these airfoils were studied for various angles of attack. It was found that the aerodynamic efficiency of the morphed airfoil was 12% higher than that of the target airfoil at  $4^\circ$  angle of attack for Reynolds number of  $3.9 \times 10^5$  and 54% rise in aerodynamic performance was noted as Reynolds number was varied from  $2.5 \times 10^5$  to  $3.9 \times 10^5$ . The morphed airfoil exhibited the nature of low Reynolds number airfoil.

Keywords: Morphing airfoil, SUAV, CFD, Low Reynolds number flow; Aerodynamics.

### 1. Introduction

In recent days, morphing research has gained momentum in the field of aerospace. The term 'Morphing' emerged from the Greek word "metamorphoses" which means transform [1]. Some of the main reasons to use wing morphing include extending the flight envelope, increasing the aerodynamic efficiency to get better range or endurance and eliminating the need for conventional control surfaces.

**Nomenclatures**

|                 |   |
|-----------------|---|
| $A$             | Area of an airfoil, $m^2$                                 |
| $C$             | Chord length of an airfoil, m                             |
| $c_d$           | Drag coefficient of an airfoil                            |
| $c_f$           | Skin friction coefficient of the flat plate               |
| $c_l$           | Lift coefficient of an airfoil                            |
| $c_p$           | Pressure coefficient of an airfoil                        |
| $c_l/c_d$       | Aerodynamic efficiency (lift-to-drag ratio) of an airfoil |
| $D$             | Drag of an airfoil, N                                     |
| $E$             | Modulus of Rigidity, $N/m^2$                              |
| $k$             | Turbulent kinetic energy, $m^2/s^2$                       |
| $L$             | Lift of an airfoil, N                                     |
| $P$             | Pressure at the point over an airfoil, $N/m^2$            |
| $P_\infty$      | Pressure in the velocity of flight, $N/m^2$               |
| Re              | Reynolds number based on chord                            |
| $Re_\theta$     | Momentum thickness Reynolds number                        |
| $Re_{\theta_c}$ | Critical Reynolds number (intermittency starts)           |
| $Re_{\theta_t}$ | Transition Reynolds number                                |
| $S$             | Strain rate magnitude, 1/s                                |
| $t$             | Time scale, s   |
| $U$             | Velocity of the flight, m/s                               |
| $U_\tau$        | Friction velocity, m/s                                    |
| $X/C$           | Non-dimensional chord length of an airfoil                |
| $Y/C$           | Non-dimensional thickness of an airfoil                   |
| $y$             | cell distance near to wall, m                             |
| $y^+$           | Non-dimensional cell distance near to wall                |

**Greek Symbols**

|           |                                   |
|-----------|-----------------------------------|
| $\gamma$  | Intermittency                     |
| $\lambda$ | Pressure gradient parameter       |
| $\mu$     | Dynamic viscosity, $N.s/m^2$      |
| $\mu_t$   | Eddy viscosity, $N.s/m^2$         |
| $\nu$     | Kinematic viscosity, $m^2/s$      |
| $\rho$    | Density, $kg/m^3$                 |
| $\tau_w$  | Shear stress at the wall, $N/m^2$ |
| $\Omega$  | Magnitude of vorticity rate, 1/s  |
| $\omega$  | Specific dissipation rate, 1/s    |

**Abbreviations**

|      |   |
|------|---|
| ABS  | Acrylonitrile Butadiene Styrene             |
| AOA  | Angle of Attack, degree                     |
| CFD  | Computational Fluid Dynamics                |
| EMC  | Elastomeric Composite                       |
| LSB  | Laminar Separation Bubble                   |
| NACA | National Advisory Committee for Aeronautics |
| SST  | Shear Stress Transport                      |
| SUAV | Small Unmanned Aerial Vehicle               |

During design, most aircrafts are optimized for a single flight condition. Morphing of the aircraft wing shape might provide solutions where the performance of aircrafts in a wider range of flight conditions are better or even near optimum, although these may be off-design conditions in the original design. Shape morphing of the wing has been classified into three types such as planform, out-of-plane and airfoil morphing [1-3]. Airfoil morphing may be done by modifying various airfoil parameters such as thickness and camber. Modifying the camber without changing aerofoil thickness is known as camber morphing [1-3].

Plenty of research is being carried out to enhance the performance of UAVs through camber morphing to improve the performance of the vehicle mostly by improving its aerodynamic efficiency and maximum lift coefficient, which in turn improve the flight performance such as range/endurance of UAV. UAV's are operated for both civil and defence purposes and the operating Reynolds number is of the order of  $10^5$  [4-7].

The multi-element (6 elements) camber morphing airfoil concept was investigated for Unmanned Aerial Vehicle application by Poonsong (2004), Seung-HeeKo et al. and Yue Wang [4-6]. In these studies, the baseline airfoil was divided into 6 elements and connected by revolute joints. The mechanism was actuated by pneumatic actuators, shape memory alloys and servomotors [4-6]. Increase in the aerodynamic efficiency was noted for the multi-element camber morphing airfoil acting as flap compared to conventional plain flap airfoils [4-6]. Poonsong [4] reported that high drag was generated by the multi-element camber morphing airfoil (9% camber airfoil - NACA 9312) due to friction on the skin. Friswell et al. [7] developed the fish bone active camber system (FishBAC) inspired by the fish skeleton. Wind tunnel testing of the FishBAC morphing airfoil showed that 20%-25% increase in the aerodynamic efficiency compared to conventional flapped airfoils [7].

Though the multi-element camber morphing airfoil concept can be applied to low-high camber modifications, the mechanism involved is too complex to actuate the elements. There is mandatory demand to develop a simple mechanism for airfoil morphing. In order to morph one airfoil into another airfoil, minimum two elements are required. The aim of the present work is to explore a two-element camber morphing concept which morphs a baseline airfoil into another airfoil to achieve high aerodynamic efficiency comparable to that of a test-case airfoil. In order to test the concept of two element camber morphing, NACA 0012 was selected as baseline airfoil based on literature [4, 7]. NACA 23012 from NACA 5-digit family was chosen as test case airfoil as it has the camber-line similar to that of the morphed airfoil and as it has the same thickness as that of the baseline airfoil. The mean-line of the NACA 0012 was morphed at 35% of the chord to achieve the shape and the aerodynamic efficiency closer to that of NACA 23012. Transient simulations were carried out with the three airfoils NACA 0012, NACA 23012 and the morphed NACA 0012 for chord based Reynolds numbers of  $2.5 \times 10^5$  and  $3.9 \times 10^5$ , using the transitional SST model in ANSYS Fluent 14.0. The lift characteristics, drag characteristics and the aerodynamic efficiency for these three airfoils were studied and reported.

## 2. Geometric and Computational Modelling

This section elaborates the mechanism for two element camber morphing concept, the geometric details of the airfoils and the simulations carried out in the low Reynolds number flows. In low Reynolds number flows, the flow remains laminar until the onset of the separation and reattaches to the surface after encountering the transition [8-12]. The region between the separation and reattachment is called as Laminar Separation Bubble (LSB) [8-12]. LSB changes the pressure distribution over the airfoil which in turn affects the lift and drag characteristics of the airfoils [13, 14]. Due to the formation of LSB, the aerodynamic performance of the airfoil at the low Reynolds number of the order of  $10^5$  differs from its performance at the Reynolds number of  $10^6$  [13]. ANSYS Fluent 14.0 was used to simulate the transient incompressible flow behaviour of low Reynolds number flow field using transitional SST turbulence model equation.

### 2.1. Two element camber morphing concept

The two-element camber morphing concept was employed to morph a baseline airfoil into another airfoil. The baseline airfoil was divided into two segments at morphing location (35% of the chord) as shown in Fig. 1. ABS plastic was proposed for developing two airfoil segments [7]. The revolute pair (Ball Bearing) was employed to connect two segments of the airfoil to the main spar which in turn was attached to the supports. The revolute pair allows the single axis rotation to two segments of airfoil at morphing location about its axis. In order to maintain the outer surface of the airfoil continuous, the flexible material (EMC) was employed as skin over the morphing location [7]. Using four bar mechanism, two elements were simultaneously actuated by a stepper motor through a gear unit as shown in Figs. 1(c) and (d). The actuation link 1 and 2 positioned at trailing and leading edges of the airfoil were constrained to have  $\pm 2$  degree rotation about morphing axis. The specification of items used for the development of the mechanism was listed in the Table 1. Geometric modelling of the two-element camber morphing airfoil was done with Autodesk Inventor [15].

**Table 1. Specifications of the items involved in mechanism.**

| Component           | Specifications                        |
|---------------------|---------------------------------------|
| Stepper Motor       | Gear type, 0.25 <sup>0</sup> inc/step |
| Spur gear (Driver)  | Diameter, $\phi=20$ mm, 40 teeth      |
| Spur gear (Driven)  | Diameter, $\phi=24$ mm, 30 teeth      |
| Ball Bearing        | $\phi=8$ mm(ID), $\phi=16$ mm(OD)     |
| EMC (flexible skin) | E=3.18 MPa [1]                        |
| ABS plastic         | E=2.345 GPa                           |

In this approach, the morphing mechanism was housed externally. In an actual system, fuselage of the SUAV holds the actuation mechanism of the morphing airfoil. The additional mass coming through actuation mechanism can be accounted into empty weight of the aircraft. In designing stage of the SUAV, the designers can account the added mass due to the morphing mechanism to design the fuselage and to select the material for airframe of the SUAV.

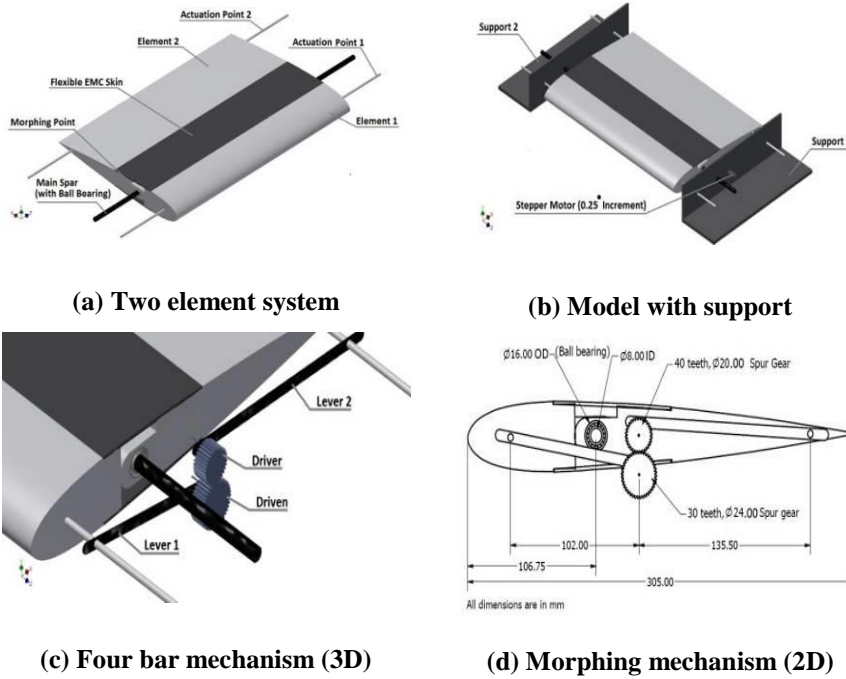


**Fig. 1. Two element camber morphing airfoil (Geometry and mechanism).**

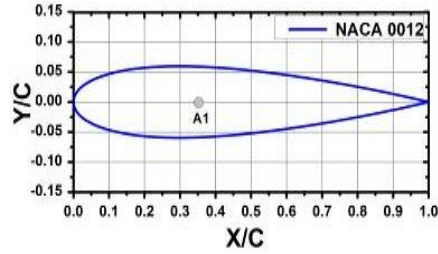
## 2.2. Airfoil geometry for simulation

A symmetric airfoil (NACA 0012) and an asymmetric airfoil (NACA 23012) were selected as baseline and test-case airfoil respectively to investigate the two-element camber morphing concept. The chord of these airfoils was 0.305meter [7, 8, 10] and same thickness was used for these airfoils to employ camber morphing concept. While the NACA 0012 mean-line has no camber, NACA 23012 has camber of 2% of chord. The curvature of the mean camber-line of NACA 23012 comprises of two different parts - a cubic curve until 15% of the chord and remains linear after 15% of the chord. By morphing the mean-line of NACA 0012 at 35% of the chord (at point A1), the morphed airfoil was generated which has a comparable shape as that of NACA 23012 was shown in Figs. 2(b) and (c). The morphed NACA 0012 has a drop of  $1.5^\circ$  from point A1 towards the leading edge and the remaining portion droops down to  $2^\circ$  from point A1 to the trailing edge as shown in Fig. 2(b).

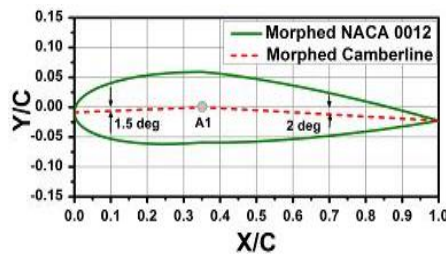
## 2.3. Governing equations for computation

CFD methods contribute to the comprehensive study of low Reynolds number flow problems. The low Reynolds number flow simulations using direct numerical simulation and large eddy simulation methods are too costly [16, 17]. Fully turbulent Reynolds-averaged Navier-Stokes type models such as one/two equations models are not suitable to capture the transitional behaviours in low Reynolds number flow simulations [17-19]. Meanwhile, the SST  $k-\omega$  model resolves the flow near the wall, but the prediction of transition or reattachment of LSBs are immature [20, 21]. Recently, the SST "Gamma-Theta" equation is developed to simulate the transition flow behaviours. Additionally, it uses two

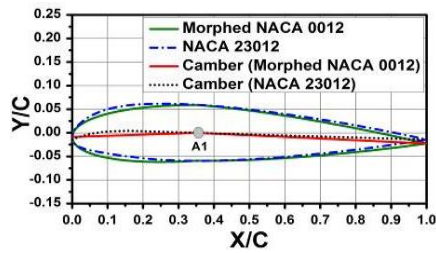
transport equations, one for the intermittency and one for the transition onset criteria in terms of momentum thickness Reynolds number. It uses a new empirical correlation to cover standard bypass transition as well as flows in low free-stream turbulence. This built-in correlation has been extensively validated together with the SST  $k-\omega$  model [22-24] for a wide range of transitional flows. It is the recommended transition model for general-purpose applications.



(a) Baseline airfoil



(b) Morphed airfoil



(c) Morphed airfoil and Target airfoil

**Fig. 2. Airfoil geometries.**

ANSYS Fluent [25], the commercial software package is used for this study and solves the unsteady Reynolds averaged Navier-Stokes equations for turbulent flow and these equations are expressed in Cartesian coordinates as follows:

$$\frac{\partial \rho}{\partial t} + \frac{\partial [\rho U_j]}{\partial x_j} = 0 \tag{1}$$

$$\frac{\partial [\rho U_i]}{\partial t} + \frac{\partial [\rho U_j U_i]}{\partial x_j} = - \frac{\partial p}{\partial x_i} + \frac{\partial \left[ \mu \left( \frac{\partial U_i}{\partial x_j} + \frac{\partial U_j}{\partial x_i} - \frac{2}{3} \delta_{ij} \frac{\partial U_l}{\partial x_l} \right) \right]}{\partial x_j} + \frac{\partial [-\rho \overline{U_i U_j}]}{\partial x_j} \tag{2}$$

Transitional SST model employed with ANSYS Fluent [25] has a few modifications compared to original SST Gamma-Theta model, in order to improve the transition predictions. These modifications are improved correlation for transition onset to predict both the natural and bypass transition, an amendment to the separation induced transition modification to prevent premature transition near the separation point and some alterations to the model coefficients in turn to improve for flow history effects on the transition onset location. The transition SST model used in ANSYS Fluent is shown below.

The transport equation for the intermittency,  $\gamma$  [25] is:

$$\frac{\partial[\rho\gamma]}{\partial t} + \frac{\partial[\rho U_j \gamma]}{\partial x_j} = P_{\gamma 1} - E_{\gamma 1} + P_{\gamma 2} - E_{\gamma 2} + \frac{\partial \left[ \left( \mu + \frac{\mu_t}{\sigma_\gamma} \right) \frac{\partial \gamma}{\partial x_j} \right]}{\partial x_j} \quad (3)$$

The transition and destruction/relaminarization sources are as follows [25]:

$$P_{\gamma 1} = 2F_{length} \rho S [\gamma F_{onset}]^{C_{\gamma 3}}; E_{\gamma 1} = P_{\gamma 1} \gamma \quad (4)$$

$$P_{\gamma 2} = (2C_{\gamma 1}) \rho \Omega \gamma F_{turb}; E_{\gamma 2} = C_{\gamma 2} P_{\gamma 2} \gamma \quad (5)$$

where  $F_{onset}$  &  $F_{turb}$  are the function controlling the onset of transition and the turbulence,  $F_{length}$  is an empirical correlation that controls the length of the transition region.

The transport equation for the transition momentum thickness Reynolds number,  $Re_{\theta_t}$  [25] is:

$$\frac{\partial[\rho Re_{\theta_t}]}{\partial t} + \frac{\partial[\rho U_j Re_{\theta_t}]}{\partial x_j} = P_{\theta_t} + \frac{\partial \left[ \sigma_{\theta_t} (\mu + \mu_t) \frac{\partial Re_{\theta_t}}{\partial x_j} \right]}{\partial x_j} \quad (6)$$

The source term is defined as follows [25]:

$$P_{\theta_t} = c_{\theta_t} \frac{\rho}{t} (Re_{\theta_t} - Re_{\theta_t}) (1 - F_{\theta_t}); t = \frac{500\mu}{\rho U^2} \quad (7)$$

The modification for separation-induced transition is [25]:

$$\gamma_{sep} = \min \left( 2 \max \left[ \left( \frac{Re_v}{3.23 Re_{\theta_c}} \right) - 1, 0 \right] F_{reattach}, 2 \right) F_{\theta_t} \quad (8)$$

$$\gamma_{eff} = \max(\gamma, \gamma_{sep}) \quad (9)$$

The transition model interacts with the SST turbulence model, is as follows [25]:

$$\frac{\partial[\rho k]}{\partial t} + \frac{\partial[\rho U_j k]}{\partial x_j} = P_k - D_k + \frac{\partial \left[ (\mu + \mu_t) \frac{\partial k}{\partial x_j} \right]}{\partial x_j} \quad (10)$$

$$P_k = \gamma_{eff} P_k; D_k = \min(\max(\gamma_{eff}, 0.1), 1) D_k \quad (11)$$

where  $P_k$  and  $D_k$  are the original production and destruction terms for the SST model and  $F_{reattach}$  and  $F_{\theta t}$  are the function controlling the reattachment and the transition onset momentum thickness. The functions controlling  $F_{onsets}$ ,  $F_{turb}$ ,  $F_{reattach}$  and  $F_{\theta t}$  are given as

$$Re_v = \frac{\rho y^2 S}{\mu}; R_T = \frac{\rho k}{\mu \omega}; Re_\omega = \frac{\rho \omega y^2}{\mu} \quad (12)$$

$$Re_{\theta t} = f(Tu, \lambda); F_{length} = f(Re_{\theta t}); Re_{\theta c} = f(Re_{\theta t}) \quad (13)$$

where  $Tu$  is the turbulent intensity,  $Re_v$  is the vorticity based Reynolds number,  $R_T$  is the viscosity ratio and  $Re_\omega$  is the turbulence dissipation rate based Reynolds number.

The constants for the intermittency and transition momentum thickness equation are [25]:

$$C_{y1} = 0.03; C_{y2} = 50; C_{y3} = 0.5; \sigma_y = 1.0; c_{\theta t} = 0.03; \sigma_{\theta t} = 2.0$$

In order to capture the LSB correctly, the grid must have a wall  $y^+$  of approximately one [8, 25]. The wall  $y^+$  value is used to find first cell distance normal to the wall. The first cell distance has to be set while meshing the geometry near the wall. By setting the value for  $y^+$ , the first cell distance can be computed approximately by Eqs. (14) and (15). The value for skin friction coefficient is approximated from the skin friction coefficient of the flat plate as shown in Eq. (14).

$$c_f = \frac{0.074}{Re^{1/5}}; \frac{\tau_w}{\rho} = \frac{1}{2} U^2 c_f \quad (14)$$

$$U_\tau = \sqrt{\frac{\tau_w}{\rho}}; y = \frac{y^+ \nu}{U_\tau} \quad (15)$$

#### 2.4. Grid generation and computational setup

The computational domain for the simulation was modelled as a C-H domain as shown in Fig. 3. The boundaries were set as far as 20 times of the chord away from airfoil [8]. The structured grid was generated over the airfoil with quadrilateral elements. The first cell distance normal to the airfoil was set to maintain the wall  $y^+$  value below one. The total number of cells in the domain was maintained close to 130,000 where the grid independence was achieved as shown in Fig. 4, which means the solution is independent of grid size. Around 500 elements were spread individually over top and bottom surface of the airfoil in the stream-wise direction. Velocity inlet, wall and pressure outlet conditions were specified as the boundary conditions for the simulation. Flight velocity of the SUAV is specified in the velocity inlet; atmospheric pressure is specified in pressure outlet and the wall defines the airfoil surface as well as ensures the no-slip condition. The solver settings are shown in the Table 2.

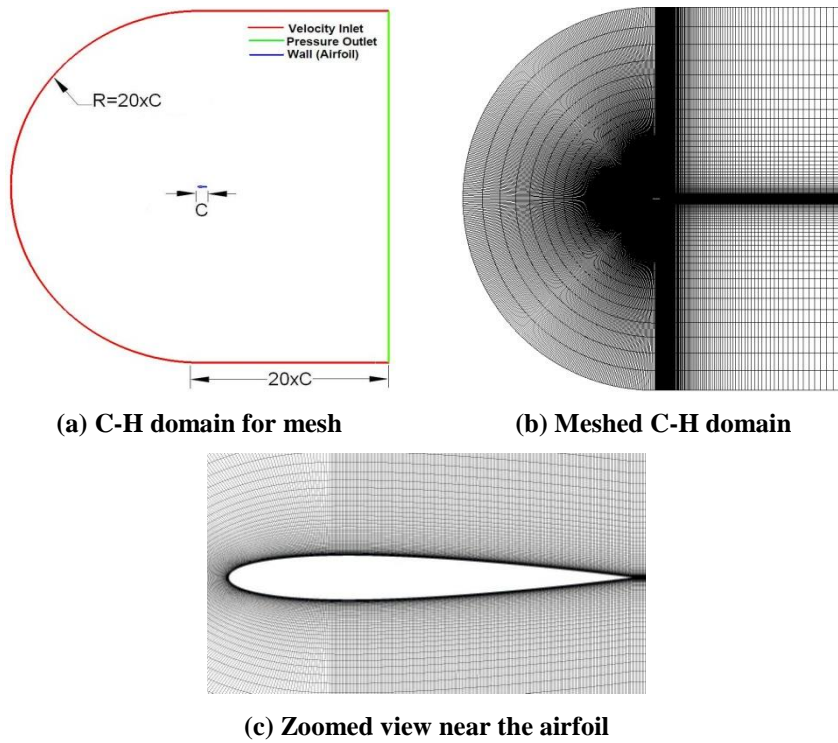


Fig. 3. Computational domain (Domain and mesh).

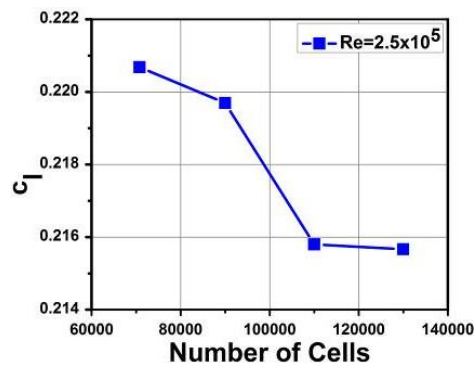


Fig. 4. Grid independence test (Number of cells vs. coefficient of lift).

Apart from using the transition SST model, the aerodynamic performance of the airfoils at the low Reynolds numbers was also computed by  $e^N$  method using XFLR5 version 6.10 [8, 9, 11] for comparison. XFLR5 solves the potential panel method and interactive boundary for the viscous effects. The “ $N$ ” factor used for the simulation was calculated using the turbulent intensity from Eq. (16) as follows

$$N = 2.13 - 6.18 \log_{10}(Tu) \quad (16)$$

The pressure coefficient distribution, lift coefficients, drag coefficients and the aerodynamic efficiency for NACA 0012, morphed NACA 0012 and NACA 23012

were computed through the simulations. The pressure coefficient, lift and drag coefficient and aerodynamic efficiency are expressed as follows [7, 12, 26, 27].

$$c_p = \frac{P - P_\infty}{\frac{1}{2}\rho U^2} \quad (17)$$

$$c_l = \frac{L}{\frac{1}{2}\rho AU^2}; c_d = \frac{D}{\frac{1}{2}\rho AU^2} \quad (18)$$

$$\frac{c_l}{c_d} = \frac{L}{D} \quad (19)$$

**Table 2. Solver settings used in ANSYS Fluent 14.0.**

| Type                         | Conditions                 |
|------------------------------|----------------------------|
| <b>Solver</b>                | Pressure Based             |
| <b>Viscous Model</b>         | SST Transition Model       |
| <b>Turbulent intensity</b>   | 0.11 %                     |
| <b>Algorithm</b>             | SIMPLE (Presto)            |
| <b>Discretization Scheme</b> | Second Order Upwind Scheme |
| <b>Fixed Time Step</b>       | $1 \times 10^{-4}$         |

### 3. Results and Discussion

#### 3.1. Validation of the computational model

The validation study was carried out for NACA 0012 airfoil exposed to the chord based Reynolds number of  $2.5 \times 10^5$ . In addition to Joshua et al. [8] as mentioned earlier, Wahidi et al. [12] used 24 pressure taps on the top surface of the airfoil and 12 pressure taps on the bottom surface of the NACA 0012 to measure the pressure distribution. Figure 5 shows a comparison of time-averaged coefficient of pressure distribution over the NACA 0012 for the  $4^\circ$  angle of attack obtained by current simulations with the results of Joshua et al. and Wahidi et al. [8, 12]. The current simulation closely matches with the study conducted in ANSYS CFX solver and it follows the trend of the published experimental study [8, 12]. The small variations in the simulations results may be due to the different number of data used for time-averaging calculations. For the time-averaging calculation, 2000 data points were taken between 1 second to 1.2 second as shown in Fig. 6. Figure 5 also shows that the results obtained through the XFLR5 by setting N factor of the  $e^N$  method to 8.1 shows the same trend as the solutions obtained from ANSYS Fluent 14.0 but there is a shift in the location of the transition point of the LSB. The formation of LSB over the airfoil surface modifies the flow curvature which changes the pressure distribution as shown in Fig. 5 and contributes to the lift and drag coefficients of the airfoils [14].

Tables 3 and 4 show the comparison of time-averaged co-efficient of lift and drag with the available published data [8, 12]. The lift coefficients of present simulation show close agreement with the published results of Joshua et al. [8]. Results from XFLR5 also follow the same qualitative trend. The low Reynolds

number flows are usually associated with the presence of LSBs over the airfoil. The published experimental data differ from the computational studies. One of the reasons may be the insufficient number of pressure ports used for the pressure measurements [10, 12]. The drag coefficients from both ANSYS Fluent 14.0 and XFLR5 follow the same trend. As the angle of attack increases, the drag coefficient increases as expected. At low angles of attack, drag coefficient of the present simulations differs from that of Joshua et al. [8].

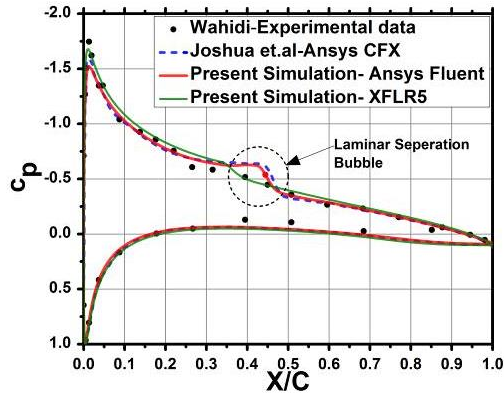
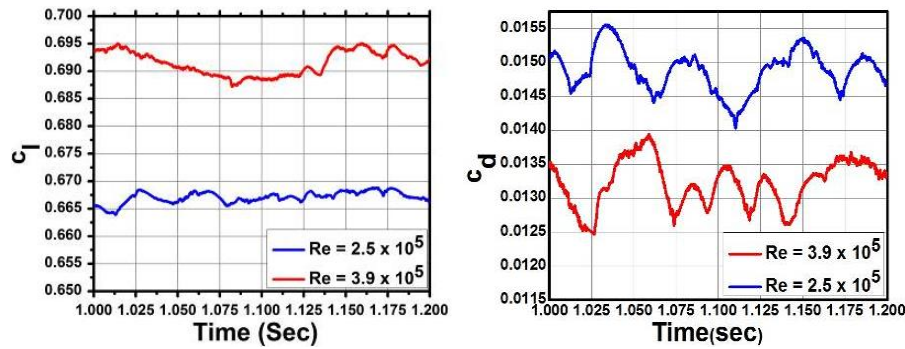


Fig. 5. Time-averaged pressure coefficient distribution over NACA 0012 at 4° AOA for  $Re = 2.5 \times 10^5$ .



(a) Lift coefficient

(b) Drag coefficient

Fig. 6. Time-averaging data- Sample of NACA 0012 at 6° AOA.

Table 3. Comparison of lift coefficient with literature data.

| AOA | Lift Coefficient   |                   |             |               |
|-----|--------------------|-------------------|-------------|---------------|
|     | Wahidi et al. [12] | Joshua et al. [8] | Present-CFD | Present XFLR5 |
| 0   | -0.1723            | 0.0006            | -0.00004    | 0.0006        |
| 4   | 0.4468             | 0.5164            | 0.5170      | 0.5522        |
| 8   | 0.8872             | 0.7672            | 0.7869      | 0.8639        |

**Table 4. Comparison of drag coefficient with literature data.**

| AOA | Drag Coefficient |             |               |
|-----|------------------|-------------|---------------|
|     | Joshua et al.    | Present-CFD | Present XFLR5 |
| 0   | 0.0168           | 0.0096      | 0.0090        |
| 4   | 0.0116           | 0.0111      | 0.0109        |
| 8   | 0.0225           | 0.0204      | 0.0171        |

### 3.2. Performance of morphed NACA 0012 with baseline and target airfoils

In this section, aerodynamic performance of the morphed NACA 0012 with baseline airfoils is presented. Figure 7 shows the comparison between time-averaged lift and drag coefficient for these three airfoils at the Reynolds number of  $2.5 \times 10^5$ . The morphed NACA 0012 produces lift coefficient similar to that of NACA 23012 up to an angle of attack  $12^\circ$ . But slight rise in drag was noted compared to that of NACA 23012. As the drag increases, the aerodynamic efficiency drops, dips below that of NACA 23012 but remains higher than NACA 0012 as shown in Fig. 9(a).

The time-averaged lift and drag coefficients of these three airfoils for the Reynolds number of  $3.9 \times 10^5$  were depicted in the Figs. 8(a) and (b). The morphed NACA 0012 shows rise in lift coefficient for the angle of attack between  $0^\circ$  to  $6^\circ$  compared to the NACA 23012 and the lift coefficient remains higher than that of the NACA 0012. At  $8^\circ$  angle of attack, lift coefficient of morphed NACA 0012 matches with that of NACA 23012 and then drops at higher angles of attack. Figure 6(b) shows that as the Reynolds number changes from  $2.5 \times 10^5$  to  $3.9 \times 10^5$ , the drag coefficients drop and all three airfoils assures the same as shown in Figs.7(b) and 8(b).

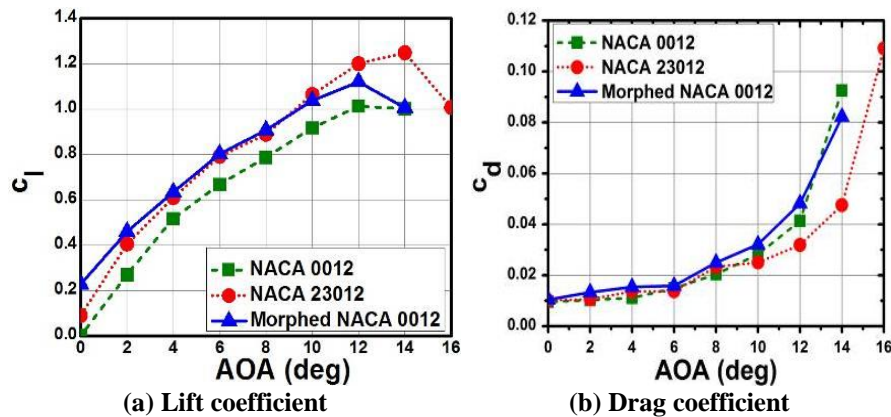


**Fig. 7. Time-averaged force coefficients for three airfoils at  $Re = 2.5 \times 10^5$ .**

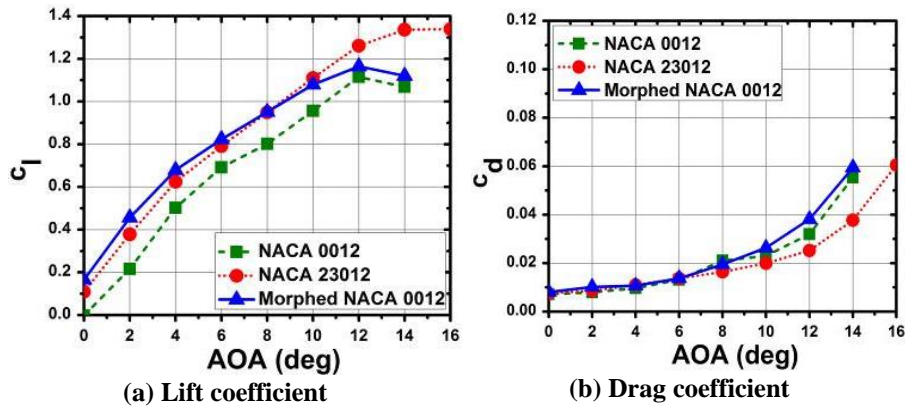


Fig. 8. Time-averaged force coefficients for three airfoils at  $Re = 3.9 \times 10^5$ .

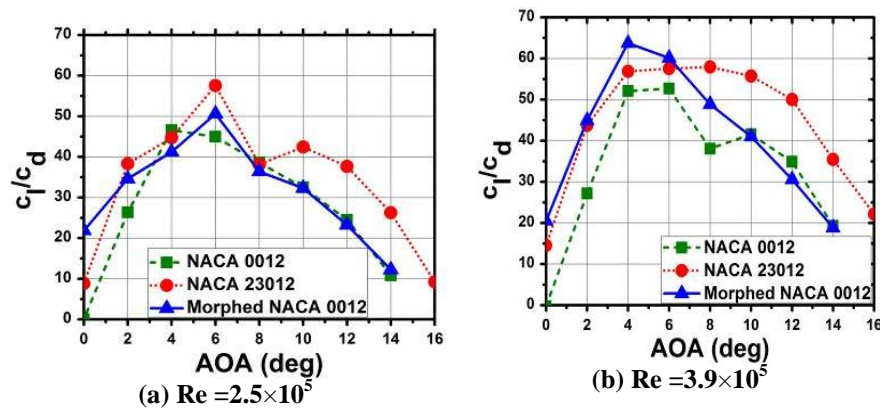


Fig. 9. Time-averaged aerodynamic efficiency of three airfoils.

The time-averaged coefficient of lift to drag ratio for three airfoils was plotted as shown in Fig. 9. The morphed NACA 0012 shows better aerodynamic efficiency than other two airfoils between angles of attack of  $0^\circ$  to  $6^\circ$  for the Reynolds number of  $3.9 \times 10^5$  as shown in Fig. 9(b). At  $4^\circ$  angle of attack, morphed NACA 0012 shows 22% and 12% increase in aerodynamic efficiency compared to NACA 0012 and NACA 23012 respectively. And above  $10^\circ$ , morphed NACA 0012 performance lies closer to NACA 0012. Increase of 54% in maximum aerodynamic efficiency was noted between the Reynolds numbers  $2.5 \times 10^5$  to  $3.9 \times 10^5$  as depicted in Fig. 10.

Based on the observations made with the Fig. 8, the time-averaged coefficient of pressure distribution for these three airfoils at  $8^\circ$  angle of attack is plotted as shown in Fig. 11. The peak pressure coefficient for morphed NACA 0012 is 39% higher than the NACA 23012 and due to rapid shape change at 35% of chord, a jump in coefficient of pressure distribution was noticed. The rise in peak pressure coefficient contributes to both lift and drag coefficient.

The time-averaged transition point locations for varying angle of attack was investigated and plotted in Fig. 12. At zero-degree angle of attack, the transition location move towards the leading edge for the morphed NACA 0012 compared to other two airfoils. Within 0° to 4° angle of attack, minimum variation in the location of transition point of morphed NACA 0012 was noted. This behaviour was exhibited by the low Reynolds Number airfoils [28-30]. It was also observed that in the operating range of angle of attack (0°- 4°), the maximum aerodynamic efficiency was attained in the narrow transition location range for the morphed NACA 0012 for Reynolds number of  $3.9 \times 10^5$ . Rise in the aerodynamic efficiency noted for the morphed airfoil between 0° to 4° angle of attack for the Reynolds number of  $3.9 \times 10^5$  and the transition location do not vary much in this region.

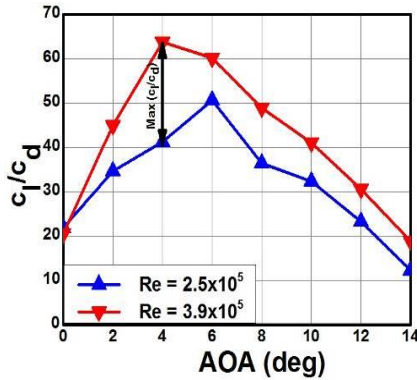


Fig. 10. Aerodynamic efficiency of morphed NACA 0012.

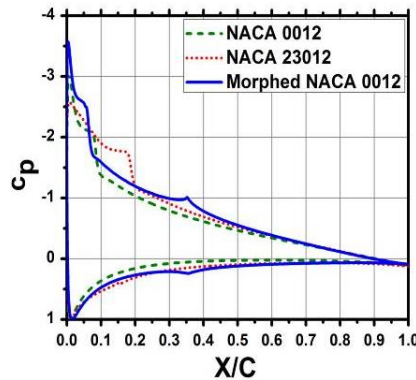


Fig. 11. Time-averaged  $c_p$  at 8° for three airfoils at  $Re=3.9 \times 10^5$ .

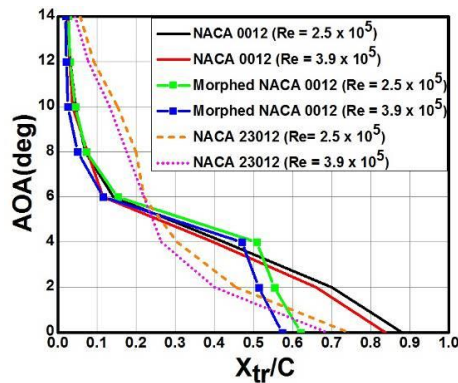


Fig. 12. Time-averaged transition location of LSB for three airfoils.

#### 4. Conclusions

The feasibility of morphing a baseline airfoil into another airfoil with same thickness was examined through two element camber morphing concept. The aerodynamic performance characteristics of these three airfoils were investigated in this paper. The following conclusions were drawn from the current study.

- Maximum aerodynamic efficiency of morphed NACA 0012 airfoil increased to 54%, at 4° angle of attack as Reynolds number increases from  $2.5 \times 10^5$  to  $3.9 \times 10^5$ .
- Morphed NACA 0012 airfoil exposed to Reynolds number of  $3.9 \times 10^5$  shows better performance than the NACA 23012 within the range of 0° to 6° angle of attack and the maximum efficiency of morphed NACA 0012 was 12% higher than the NACA 23012, at 4° angle of attack.
- The maximum aerodynamic efficiency of morphed NACA 0012 airfoil is still more than that of NACA 0012 for Reynolds number of  $2.5 \times 10^5$ , but is less than that of NACA 23012, which is the target airfoil.
- The morphed NACA0012 airfoil exhibited the nature of low Reynolds number airfoil by showing minimum variation in location of transition point for angles of attack from 0° to 4° and in this narrow transition point location range, the maximum aerodynamic efficiency was attained quickly for Reynolds number of  $3.9 \times 10^5$ .
- Increase in the maximum aerodynamic efficiency of the morphed airfoil shows that this morphing is beneficial to attain a higher range, endurance and shallower glide path at a Reynolds number of  $3.9 \times 10^5$ .
- Within the typical operating angle of attack, the morphed configuration (morphed NACA 0012) shows the equivalent performance as test-case configuration (NACA 23012). This idea can be extended to morph the same thickness airfoils among the low Reynolds number family.
- Two element morphing mechanism can be preferred over higher element morphing mechanism for low camber airfoil morphing applications. As the morphing mechanism is housed externally from the wing assembly, the added mass can be accounted in empty weight of the vehicle during design stage.
- This two-element camber morphing concept was employed to morph a baseline airfoil into another low cambered airfoil (2% camber with respect to baseline airfoil). The further studies are needed to explore the limit of this concept for which the morphed configuration will produce favourable aerodynamic efficiency.

## References

1. Barbarino, S.; Bilgen, O.; Friswell, M.I.; Ajai, R.M.; and Inman, D.J. (2010). A review of morphing aircraft. *Journal of Intelligent Material Systems and Structures*, 22(9), 823-877.
2. Friswell, M.I. (2014). Morphing aircraft: an improbable dream? *Proceedings of the ASME 2014 Conference on Smart Materials, Adaptive Structures and Intelligent Systems*, Newport, Rhode Island, USA, 1-7.
3. Vasista, S.; Tong, L.; and Wong, K.C. (2012). Realization of morphing wings: a multidisciplinary challenge. *Journal of Aircraft*, 49(1), 11-28.
4. Poonsong, P. (2004). *Design and analysis of a multi-section variable camber wing*. MSc. Thesis. University of Maryland, College Park, MD 20742, United States.

5. Ko, S.H.; Bae, J.S.; and Rho, J.H. (2014). Development of a morphing flap using shape memory alloy actuators: the aerodynamic characteristics of a morphing flap. *Smart Materials and Structures*, 23(7), 1-21.
6. Wang, Y. (2015). *Development of flexible-rib morphing wing system*. M.Sc. Thesis. University of Toronto, 27 King's College Cir, ON M5S, Canada.
7. Woods, B.K.S.; Bilgen, O.; and Friswell, M.I. (2014). Wind tunnel testing of the fish bone active camber morphing concept. *Journal of Intelligent Material Systems and Structures*, 25(7), 772-785.
8. Council, J.N.N.; and Boulama, K.G. (2013). Low-Reynolds-number aerodynamic performance of NACA 0012 and Selig-Donovan 7003 airfoils. *Journal of Aircraft*, 50(1), 204-216.
9. XFLR5 ver. 6.10.04 (2014). Retrieved on September 27, 2015, from <http://www.xflr5.com/xflr5.htm>
10. Selig, M.S.; Deters, R.W.; and Williamson, G.A. (2011). Wind tunnel testing airfoils at low Reynolds numbers. *49<sup>th</sup> AIAA Aerospace Sciences Meeting*, Orlando, FL, 1-32.
11. Van Ingen, J.L. (2008). The  $e^N$  method for transition prediction. Historical review of work at TU Delft. *38<sup>th</sup> Fluid Dynamics Conference and Exhibit*, Seattle, Washington, 1-49.
12. Wahidi, R.; and Bridges, D.H. (2009). Experimental investigation of the boundary layer and pressure measurements on airfoil with laminar separation bubbles. *39<sup>th</sup> AIAA Fluid Dynamics Conference*, San Antonio, Texas.
13. Muller, T.J. (1999). *Aerodynamic measurements at low Reynolds numbers for fixed wing micro aerial vehicles*. University of Notre Dame, Notre Dame, IN 46556, USA, 1-32.
14. Hansen, K.L.; Kelso, R.M.; Choudhry, A.; and Arjomandi, M. (2014). Laminar separation bubble effect on the lift curve slope of an airfoil. *19<sup>th</sup> Australasian Fluid Mechanics Conference*, Melbourne, Australia.
15. Autodesk Inventor user guide (2010). Retrieved on 27<sup>th</sup> September 2015, from <http://inventortutorials.blogspot.in/>
16. Alam, M.F.; Walters, K.; and Thompson, D.S. (2011). Simulations of separated flow around an airfoil with ice shape using hybrid RANS/LES Models. *29<sup>th</sup> AIAA Applied Aerodynamics Conference*, Honolulu, Hawaii, 1-12.
17. Schobeiri, M.T.; and Nikparto, A. (2014). A comparative numerical study of aerodynamics and heat transfer on transitional flow around a highly-loaded turbine blade with flow separation using RANS, URANS and LES. *ASME-Turbo Expo 2014: Turbine Technical Conference and Exposition*, Düsseldorf, Germany, 1-13.
18. Rumsey, C.L.; and Greenblatt, D. (2009). Flow control predictions using unsteady Reynolds-averaged Navier-Stokes modelling: a parametric study. *AIAA Journal*, 47(9), 2259-2262.
19. Council, J.N.N.; and Boulama, K.G. (2011). Validating the URANS shear stress transport  $\gamma-Re_\theta$  model for low-Reynolds-number external aerodynamics. *International Journal for Numerical Methods in Fluids*, 69(8), 1411-1432.

20. Zheng, X.; Liu, C.; Liu, F.; and Yang, C.I. (1998). Turbulent transition simulation using the  $k-\omega$  model. *International Journal for Numerical Methods in Engineering*, 42 (5), 907-926.
21. Savill, A.M. (1992). A synthesis of T3 test case predictions. *Cambridge Univ. Press*, Cambridge, England, U.K., 404-442.
22. Menter, F.R.; Langtry, R.B.; Likki, S.R.; Suzen, Y.B.; Huang, P.G.; and Völker, S. (2006). A correlation based transition model using local variables part 1-model formulation. *ASME-Journal of Turbo machinery*, 128 (3), 413-422.
23. Langtry, R.B.; Menter, F.R.; Likki, S.R.; Suzen, Y.B.; Huang, P.G.; and Völker, S. (2006). A correlation based transition model using local variables part 2 - test cases and industrial applications. *ASME-Journal of Turbo machinery*, 128 (3), 423-434.
24. Langtry, R.B.; and Menter, F.R. (2005). Transition modeling for general CFD applications in aeronautics. *43<sup>rd</sup> AIAA Aerospace Sciences Meeting and Exhibit*, Reno, Nevada, 277-303.
25. ANSYS Fluent User's Guide (2014). Retrieved on November 5, 2014, from <http://www.afs.enea.it/project/neptunius/docs/fluent/html/th/node74.htm>
26. Raymer, D.P. (1992). *Aircraft design: A conceptual approach* (2<sup>nd</sup> ed.). Washington: AIAA.
27. Hale, F.J. (1984). *Introduction to aircraft performance, selection and design*. (1<sup>st</sup> ed.). New York: John Wiley & Sons Inc.
28. Cole, G.M.; and Muller, T.J. (1990). *Experimental measurements of the laminar separation bubble on an Eppler 387 airfoil at low Reynolds numbers*. University of Notre Dame, Final Report UNDS-1419-FR, Notre Dame, Indiana.
29. Selig, M.S. (2003). *Low Reynolds number airfoil design lecture notes*. University of Illinois at Urbana-Champaign, Urbana, Illinois 61801, USA
30. Boutilier, M.S.H.; and Yarusevych, S. (2011). Effect of end plates and blockage on low Reynolds number airfoil experiments. *41<sup>th</sup> AIAA Fluid Dynamics Conference and Exhibit*, Honolulu, Hawaii, 1547-1559.